PHYSICAL REVIEW MATERIALS **8**, 054003 (2024)

Intrinsic high-temperature ferroelectricity, superferroelasticity, and deep-ultraviolet nonlinear optical response of GaOCl monolayer

Zhengyuan Tu,[1,4,*] Yunhua Wang,[2,3,*,†] Weitu Liao,[3] Tao Hu,[3] and Shengjun Yuan[3,4,‡]
[1]*Shenzhen JL Computational Science and Applied Research Institute, Shenzhen, 518131, China*
[2]*Lanzhou Center of Theoretical Physics & Key Laboratory for Quantum Theory and Applications of the Ministry of Education & Key Laboratory of Theoretical Physics of Gansu Province & School of Physical Science and Technology, Lanzhou University, Lanzhou 730000, China*
[3]*Key Laboratory of Artificial Micro- and Nano-structures of Ministry of Education and School of Physics and Technology, Wuhan University, Wuhan 430072, China*
[4]*Beijing Computational Science Research Center, Beijing, 100193, China*

(Received 6 February 2024; revised 11 April 2024; accepted 9 May 2024; published 21 May 2024; corrected 6 June 2024)

Two-dimensional materials with coexisting multifunctional properties offer platforms for revealing multifield coupling physics in both lower dimension and symmetry, and enable the potential application demand for multifunctional devices in nanoelectronics. Preceding theoretical and experimental investigations show that layered metal oxyhalides (MOX) have diverse functional properties such as the visible-light-active photocatalyst in Bi-based system as well as the magnetic and electron-correlated properties in transition-metal-based regime. Here, applying first-principles calculations and time-dependent perturbation theory, we identify that GaOCl monolayer has intrinsically multiple functional characteristics including high-temperature ferroelectricity, superferroelasticity, and strong deep-ultraviolet nonlinear optical response. Our calculations indicate that GaOCl monolayer has a ultrawide direct band gap comparable with the third-generation semiconductors, a moderate energy barrier of ferroelectric polarization reversal but with a high Curie temperature, a superferroelasticity attributed to the largely tunable ionic radius ration of Ga^{3+} and O^{2-}, and remarkable nonlinear shift and injection currents inside deep-ultraviolet frequencies. These intrinsical multifunctional properties render GaOCl monolayer possible applications on ultrathin multifunctional nanoelectronics such as integrated multiferroic devices and ultraviolet optoelectronic devices.

DOI: 10.1103/PhysRevMaterials.8.054003

I. INTRODUCTION

The electric-field-switchable spontaneous polarization and thin thickness ranging from ten to few hundreds nanometers enable thin-film ferroelectric materials to possess important applications on modern nanoelectronics and information technology [1]. Ferroelectricity emerging in two-dimensional (2D) materials further pushes ultrathin monolayer ferroelectricity and van der Waals ferroelectricity including bilayer and multilayer with or without a twist, namely, 2D ferroelectricity, into current research focuses [2–20]. These 2D ferroelectric materials have naturally stable 2D crystal structures with intrinsically ultrathin thickness, easy fabrication by molecular beam epitaxy or mechanical exfoliation, highly tunable spontaneous polarization vectors including both in-plane and out-of-plane components, excellent compatibility with nowadays integration nanotechnology and coexisting multiple functional properties. It is highly possible that 2D ferroelectricity can overcome the critical thickness limit of ferroelectricity surviving, the abrupt changes of structures and chemical components at interfaces, oxygen vacancy defects and complex fabrication processes of ferroelectric thin-film materials. Recently, researchers have prepared various 2D ferroelectric materials such as SnTe [21], $CuInP_2S_6$ [22], In_2Se_3 [23,24], d1T-$MoTe_2$ [25], bis lead tetrachloride [26], two/three-layer WTe_2 [27], graphene/h-BN moiré heterostructure [28], twisted bilayer h-BN [29], sliding h-BN bilayer [30], transition metal dichalcogenides bilayer [31], antiferromagnet $CuCrP_2S_6$ [32], γ-GaSe [33], and bismuth layer [34]. Their ferroelectricity can be characterized by measuring the typical hysteresis loop between polarization and an electric field. First-principles calculations, free energy model, molecular dynamics, and group theory are adopted to theoretically predict plenty of 2D ferroelectric materials and their functional properties. Some new ferroelectric phenomena and mechanisms are revealed in van der Waals ferroelectric materials, such as the vertical dipole order induced by the coupling between conducting states and valley phonons [35], the symmetry-locked out-of-plane and in-plane polarization [24], the in-plane electrical polarization induced by ionic-potential anharmonicity [36], the frustrated electric dipole order [37], layer-dependent ferroelectricity [38,39], and stacking/sliding ferroelectricity [27–31,40–46]. Multifunctional properties coexisting and their couplings in 2D ferroelectricity also have interesting physics and important applications, such

---

[*] These authors contributed equally to this work.
[†] wangyunhua@lzu.edu.cn
[‡] s.yuan@whu.edu.cn

as the magnetoelectric coupling multiferroicity [47–54], the ferroelectricity-ferroelasticity multiferroicity [55–65], the ferroelectricity-manipulated transports [66,67], and the ferroelectric nonlinear optical response [68–76]. Especially, 2D materials with broadband optical response, large nonlinear optical susceptibilities and harmonic generation enable the promising on-chip photonic and optoelectronic applications [77,78].

Layered metal oxyhalides together with their 2D counterparts have diverse functional properties and potential applications. Layered bismuth oxyhalides (BiOX, where $X =$ Cl, Br, I) have a band gap of 1–3 eV [79,80], the remarkable visible light absorption [79,81] and the enhanced mobility of photo-generated carrier [81,82]. Consequently, BiOX are excellent visible-light-active photocatalysts including water splitting, toxic pollutants decomposition and CO_2 reduction [82–90], which are used for environmental protections and sustainable energy sources. Transition-metal oxyhalides (TMOX) and their few layer structures have intriguing magnetic, multiferroic and electron-correlated properties for spintronic applications and for revealing correlation physics. CrOX monolayers display intrinsically ferromagnetic semiconducting behavior with Curie temperature of about 150 K from theoretical calculations [91], where its spin exchange coupling is tunable by strain [92], and its half-metallicity is possibly formed by doping [93]. Layered CeOI is an antiferromagnetic Mott insulator [94], and TiOX has a Mott insulating states from Hubbard interactions [95]. VOX (X = Cl, Br) monolayers have theoretically antiferromagnetic ferroelastic properties [96], Both VOF and VOF_2 monolayers have theoretically ferromagnetic ferroelectric multiferroic properties [97,98], and Cu_2OCl_2 has magnetoelectric multiferroic property with intrinsic magnetic and ferroelectric couplings in experiments [99]. Recently, VOCl monolayer has been synthesized by the chemical exfoliation method [100], and magnetic characterization provides an evidence for magnetic order in this material. Antiferromagnetic FeOCl monolayer predicted theoretically [101] has also been fabricated by the recently developed chemical vapor transport approach [102], and the optical and electrical measurements show highly in-plane anisotropic property owing to its low structural symmetry. The rare-earth oxyhalide monolayers are theoretically predicted to be dynamically stable and have a wide band gap of 3–6 eV with remarkable linear optical absorptions [103]. The structural, electronic, piezoelectric, dielectric, thermal, and photocatalytic properties for some other metal oxyhalide monolayers have been investigated from first-principles calculations [104–107]. The Carrier mobility, doping-induced ferromagnetism, and piezoelectricity of the GaOCl monolayer are also predicted from first-principles calculations [108].

However, few works are performed on the ferroelectric, ferroelastic, and nonlinear optical properties of metal oxyhalide monolayers. Using first-principles calculations, Monte Carlo (MC) simulations and time-dependent perturbation theory, we identify that GaOCl monolayer has intrinsically multiple functional characteristics including high-temperature ferroelectricity, superferroelasticity, and strong deep-ultraviolet nonlinear optical response. Calculated results from structural relaxation, molecular dynamics, and phonon spectrum indicate that GaOCl monolayer is energetically, thermodynamically and dynamically stable, and the electronic structure and electron density calculations show a ultrawide direct band gap of 4.28 eV as a consequence of high electronegativity of Cl and O. The Berry phase based spontaneous polarization computation and the simulation of the polarization reversal kinetic process verify the 2D ferroelectricity of GaOCl monolayer, and both molecular dynamics (MD) and MC simulations show its high Curie temperature. The solid-state nudged elastic band (SSNEB) calculations verify that GaOCl monolayer can sustain several structural phase transitions because of the largely tunable ionic radius ration of Ga^{3+} and O^{2-}, enabling its superferroelasticity property. The broken inversion symmetry and ultrawide band gap indicate that GaOCl monolayer has potential second-order nonlinear optical characteristics. Therefore we apply time-dependent perturbation theory together with the Wannier interpolation method to calculate its second-order nonlinear optical conductivity. The calculated results show remarkable nonlinear shift and injection conductivities inside deep-ultraviolet frequency range, rendering GaOCl monolayer potential applications in integrated ultraviolet optoelectronic devices.

II. COMPUTATIONAL METHODS

The density functional theory (DFT) calculations are performed by using the projector-augmented wave (PAW) formalism and the Perdew-Burke-Ernzerhof (PBE) generalized gradient approximation as implemented in Vienna *ab initio* simulation package (VASP 5.4) [109–112]. All the structures are optimized by conjugate gradient method with asymmetric constraints. The plane wave energy cutoff is 500 eV, and the convergence criteria for energy and force are 10^{-4} eV and 0.001 eV/Å, respectively. The thickness of the vacuum layer is set at 30 Å to avoid artificial interaction between images of different periods. Van der Waals interactions through the Grimme correction is taken into account for bulk structure. We also use Monkhorst-Pack method [113] and use a 5 × 6 × 1 grid for k-point sampling. The SSNEB method [114] is used to search the switching pathways and determine the upper limit of energy barriers, and the Berry phase method [115] is used to evaluate polarization. The Heyd-Scuseria-Ernzerhof (HSE06) hybrid functional [116] is employed to calculate the more accurate band structures and density of states. Molecular dynamics simulations are performed within the NVT ensemble with the time step of 2 fs at different temperature. The 4 × 3 supercell of GaOCl monolayer is equilibrated for 10 ps with 5000 steps [117]. The Monte Carlo simulations of the effective Hamiltonian are performed in a periodically repeated box of 15 × 15 × 1 unit cells. We adopt the mean field theory to describe the interaction between modes. In order to get reliable results for atomic displacements, we perform at least 20 000 MC sweeps for thermalization, followed by at least 2000 additional sweeps to compute thermal averages. For calculations on phonon spectrum, the unit cell is extended into 4 × 4 × 1 supercells, a 2 × 2 × 1 k-point sampling is used, the convergence criteria for energy is set as 10^{-8} eV/Å, and the plane wave cutoff energy is set as 600 eV.

Responding to the light illumination with its time-dependent electric field $E_b(t) = E_b(\omega)e^{i\omega t} + E_b(-\omega)e^{-i\omega t}$, during transitions the position variations and the

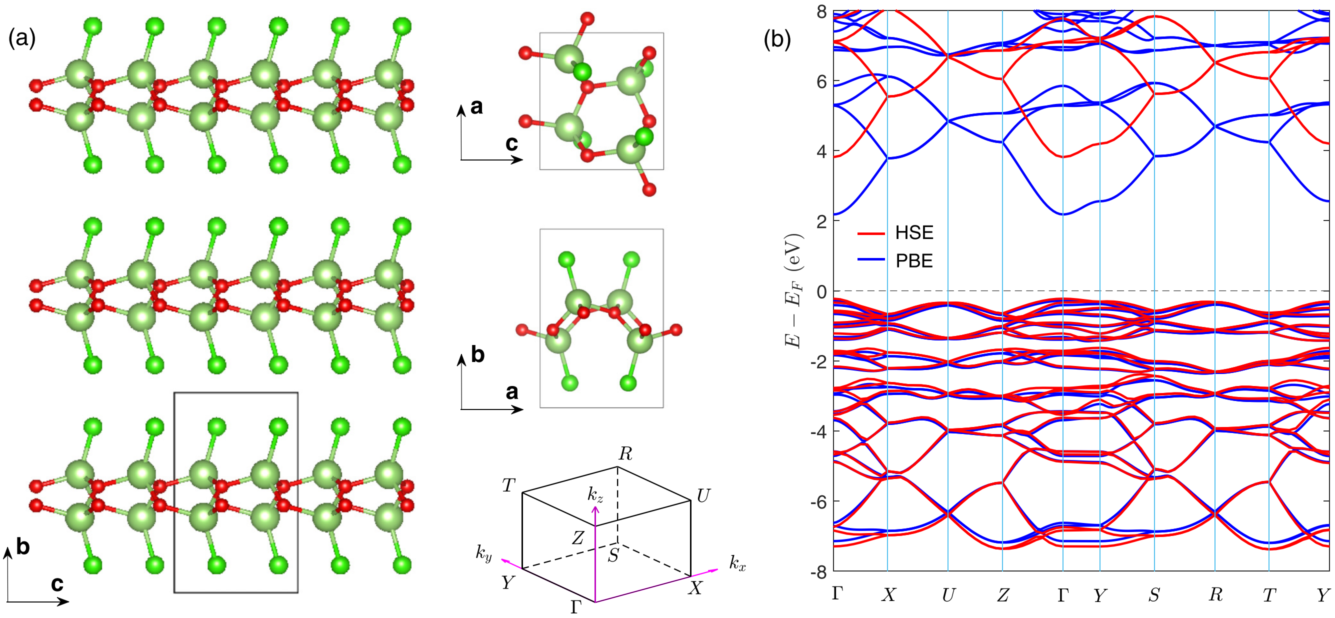

FIG. 1. (a) Different views of GaOCl bulk, where the red, green, and cyan balls represent O, Cl, and Ga atoms, respectively. The middle inset shows the first Brillouin zone with corresponding high-symmetry k points. (b) The energy band diagram of GaOCl bulk, where the blue and red lines represent the results of PBE and HSE, respectively, and the calculated band gaps based on PBE and HSE are correspondingly 2.46 and 4.04 eV.

asymmetrical injection rates for electrons in materials with broken inversion symmetry correspondingly produce the second-order shift photocurrent $j_c^{shi}(0,\omega,-\omega) = \sigma_{c;ab}^{shi}(0,\omega,-\omega)E_a(\omega)E_b(-\omega)$ and the injection photocurrent $j_c^{inj}(0,\omega,-\omega) = \eta_{c;ab}^{inj}(0,\omega,-\omega)E_a(\omega)E_b(-\omega)$, where $\sigma_{c;ab}^{shi}$ and $\eta_{c;ab}^{inj}$ are the third-rank optical conductivity tensors. Within the framework of time-dependent perturbation theory, $\sigma_{c;ab}^{shi}$ and $\eta_{c;ab}^{inj}$ during the interband transitions, i.e., $\omega \neq 0$, read [68,70,118–121]

$$\begin{aligned}\sigma_{c;ab}^{shi}(0,\omega,-\omega) = &-\frac{\pi e^3}{\hbar^2}\int_{\mathbf{k}}\sum_{n,m}\mathrm{Im}\big[r_{mn}^{a}(\mathbf{k})r_{nm,c}^{b}(\mathbf{k})\big]\\ &\times f_{nm}\delta(\omega_{mn}-\omega),\\ \eta_{c;ab}^{inj}(0,\omega,-\omega) = &-\frac{2\pi e^3\tau}{\hbar^2}\int_{\mathbf{k}}\sum_{n,m}\Delta_{mn}^{c}(\mathbf{k})r_{nm}^{b}(\mathbf{k})r_{mn}^{a}(\mathbf{k})\\ &\times f_{nm}\delta(\omega_{mn}-\omega).\end{aligned}\tag{1}$$

Here, $\int_{\mathbf{k}} = \int d^{\nu}\mathbf{k}/(2\pi)^{\nu}$ with ν as the dimension; $r_{mn}^{a}(\mathbf{k}) = v_{mn}^{a}(\mathbf{k})/(i\omega_{mn})$ is the interband dipole matrix, i.e., interband Berry connection, where $\hbar v_{mn}^{a}(\mathbf{k}) = \langle m|\partial_{k_a}H(\mathbf{k})|n\rangle$, and $\hbar\omega_{mn} = \mathcal{E}_m(\mathbf{k}) - \mathcal{E}_n(\mathbf{k})$ with Hamiltonian $H(\mathbf{k})$ and energy $\mathcal{E}_m(\mathbf{k})$ as a function of wave vector $\mathbf{k}$; $r_{nm;c}^{b}$ is the covariant derivative of r_{nm}^{b} with respect to k_c; $f_n = 1/[e^{(\mathcal{E}_n(\mathbf{k})-\mu)/(k_BT)}+1]$ is the Fermi distribution with the chemical potential μ, temperature T and $f_{nm} = f_n - f_m$; τ is the relaxation time; and $\Delta_{mn}^{c}(\mathbf{k}) = v_{mm}^{c}(\mathbf{k}) - v_{nn}^{c}(\mathbf{k})$ is difference between the group velocity $v_{mm}^{c}(\mathbf{k})$ of the mth band and the group velocity $v_{nn}^{c}(\mathbf{k})$ of the nth band.

We adopt the WANNIER90 package [122] to construct the tight-binding Hamiltonian in the Wannier representation within a given energy window, through projecting the Bloch wavefunctions from the DFT calculations onto the maximally localized Wannier functions. The position operator $\langle\mathbf{0}i|\hat{r}|\mathbf{R}j\rangle$, Wannier centers $\langle\mathbf{0}i|\hat{r}|\mathbf{0}j\rangle$, and hopping energy $\langle\mathbf{0}i|\hat{H}|\mathbf{R}j\rangle$ in the Wannier basis are the output after the Wannier function interpolation. Using the eigen states of the Wannier tight-binding Hamiltonian, Wannier position operator, and Wannier centers, we construct the Berry connection matrices and their covariant derivatives in the Hamiltonian gauge for the calculations on the nonlinear optical conductivity in Eq. (1).

III. RESULTS AND DISCUSSIONS

A. Crystal structure and band structure of GaOCl bulk

Metal chalcogens halides have been widely investigated for their rich structures and properties. For layered metal oxyhalides, there are four general structural types including FeOCl, GaOCl, PbFCl, and SmSI structures with $Pmmn$, $Pca2_1$, $P4/nmm$, $P6_3/mcm$ symmetries respectively, which are fabricated by controlling the ratio of the M^{3+} ionic radius to the O^{2-} ionic radius (i.e., $r_{M^{3+}}/r_{O^{2-}}$) [123]. The smallest ratio with $r_{M^{3+}}/r_{O^{2-}}$ between 0.35 and 0.44 produces the GaOCl structure. After the structural relaxation, the calculated GaOCl bulk is shown in Fig. 1(a). The calculated lattice constants are correspondingly 5.74, 8.35, and 5.15 Å along a, b, and c directions, which are consistent with the corresponding experimental values 5.65, 8.33, and 5.08 Å from the powder diffraction line intensity analysis [123]. As we can see, each unit cell has four units of the chemical formula, in which Ga ions locate at a slightly distorted tetrahedron coordinated to three O^{2-} and one Cl^{-}. The O^{2-} vertices of the tetrahedra are linked together in puckered layers perpendicular to the c axis, and each O^{2-} is shared by three tetrahedra. The Cl^{-} vertices are unshared and lie on alternating sides of the Ga-O net along

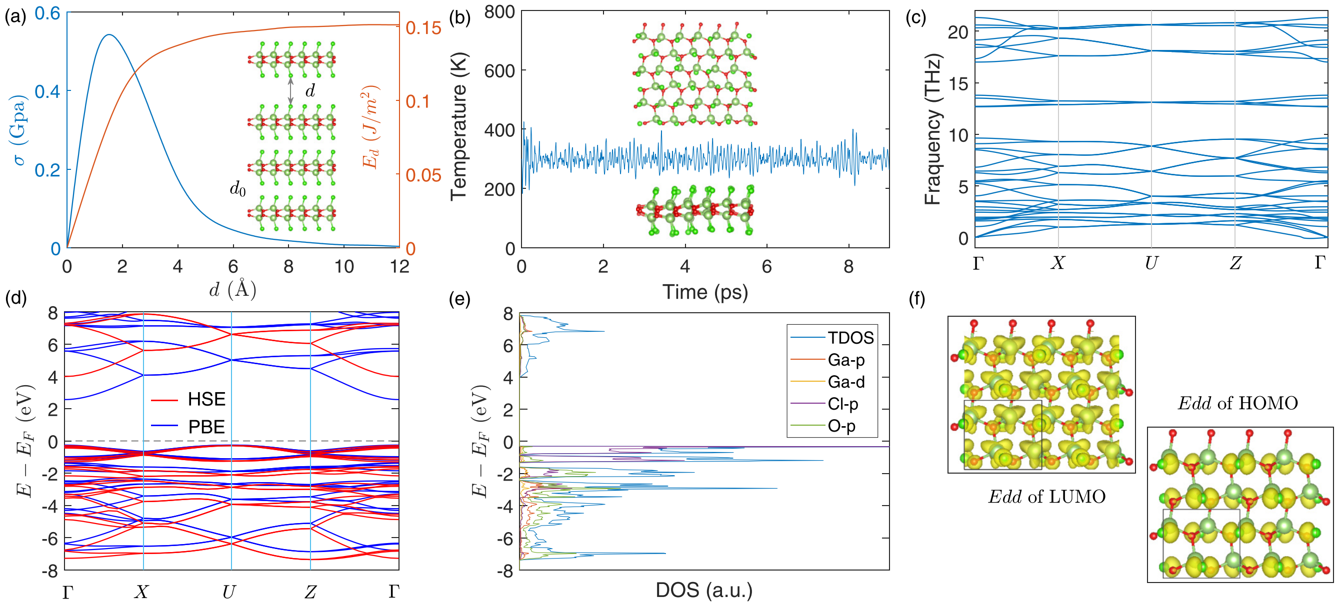

FIG. 2. (a) Cleavage energy $E_d(d) = E(d) - E(d_0)$ with energy $E(d)$ of the system and cleavage strength $\sigma(d) = \partial E_d(d)/\partial d$ of GaOCl bulk as a function of cleavage distance d with respect to the original distance d_0, where the inset represents the process of exfoliating one monolayer from the bulk. (b) Molecular dynamics simulations at 300 K with snapshots of stable structure of GaOCl monolayer from different views in the insets. (c) Calculated phonon dispersion spectrum of GaOCl monolayer showing no imaginary frequencies. (d) Electronic band structures (PBE and HSE06) of GaOCl monolayer along the path of high-symmetry points in the first Brillouin zone. (e) Density of states (DOS) of GaOCl monolayer with the corresponding total (TDOS) and projected components. (f) Electron density distributions (*Edd*) of LUMO and HOMO.

the given row of tetrahedra and induce the central symmetry breaking along the c axis. The GaOCl bulk consists of the AA-stacked layers by van der Waals interactions.

The calculated energy bands from PBE and HSE are plotted in Fig. 1(b), where the band path inside the first Brillouin zone is given in Fig. 1(a). The conduction band bottom and the valence top are at the same Γ point, and the calculated band gaps from PBE and HSE is 2.46 and 4.04 eV, respectively. Therefore the GaOCl bulk is a wide band gap semiconductor with a direct band gap.

B. Cleavage simulation, phonon spectrum, and electronic structures of GaOCl monolayer

Similar to other van der Waals laminated materials, GaOCl monolayer can be obtained from its bulk counterpart via mechanical cleavage or liquid-phase exfoliation processes [124]. Here the cleavage process is simulated through a model system containing four GaOCl monolayers in Fig. 2(a). With the increasing cleavage distance d with respect to the original distance d_0, the cleavage energy E_d with its definition of $E_d = E(d) - E(d_0)$ [125] and the cleavage strength σ defined as $\sigma = \partial E_d/\partial d$ as a function of d are calculated and plotted in Fig. 2(a). As we can see, when the cleavage distance d is close to 12 Å, E_d and σ change very little. The final cleavage energy is 0.15 J/m^2 and the cleavage strength is 0.54 GPa, which are comparable to those (0.37 J/m^2 and 2.10 GPa) for graphene exfoliated from graphite [126]. In this respect, the monolayer exfoliation from GaOCl bulk is experimentally feasible. The obtained lattice constants for GaOCl monolayer are 5.74 and 5.16 Å along a and c directions, respectively. The very little structural change for isolated monolayer GaOCl compared with its bulk counterpart indicates the weak vdW interaction between neighboring layers.

Figure 2(b) shows the first-principles molecular dynamics simulations of GaOCl monolayer at 300 K temperatures for 9 ps. As we can see, GaOCl monolayer still maintains its structural integrity without broken bonds, and the temperature fluctuation is small. Therefore GaOCl monolayer is thermodynamically stable at room temperature. Our further calculated results show that the basic framework of GaOCl monolayer is still well maintained at 900 K but broken at 1100 K, which indicates the melting point of GaOCl monolayer is around 1000 K. The dynamically stability of GaOCl monolayer is also confirmed by the absence of imaginary frequency phonon from the phonon dispersion spectrum as shown in Fig. 2(c). We further calculate the elastic constants of GaOCl monolayer and obtain $C_{11} = 43.7$, $C_{22} = 53.1$, $C_{12} = 8.7$, $C_{21} = 8.7$, and $C_{66} = 23.7$ N/m, respectively. We find that $C_{11}C_{22} > C_{12}C_{21}$ and $C_{66} > 0$, which satisfy the criteria of mechanical stability for 2D materials. Therefore GaOCl monolayer is mechanically stable.

The electronic structures of GaOCl monolayer are calculated by using both PBE and HSE, and the results are shown Fig. 2(d) with its density of states in Fig. 2(e). A wider direct band gap is 4.28 eV for GaOCl monolayer than the band gap 4.04 eV of its bulk. The ultrawide direct band gap is inside the range of the third-generation semiconductors GaN (3.4 eV) and Ga_2O_3 (4.8 eV) [127]. Therefore GaOCl monolayer have possibly potential applications in integrated ultraviolet optoelectronic devices and higher breakdown performance electronic devices, due to its large band gap energy

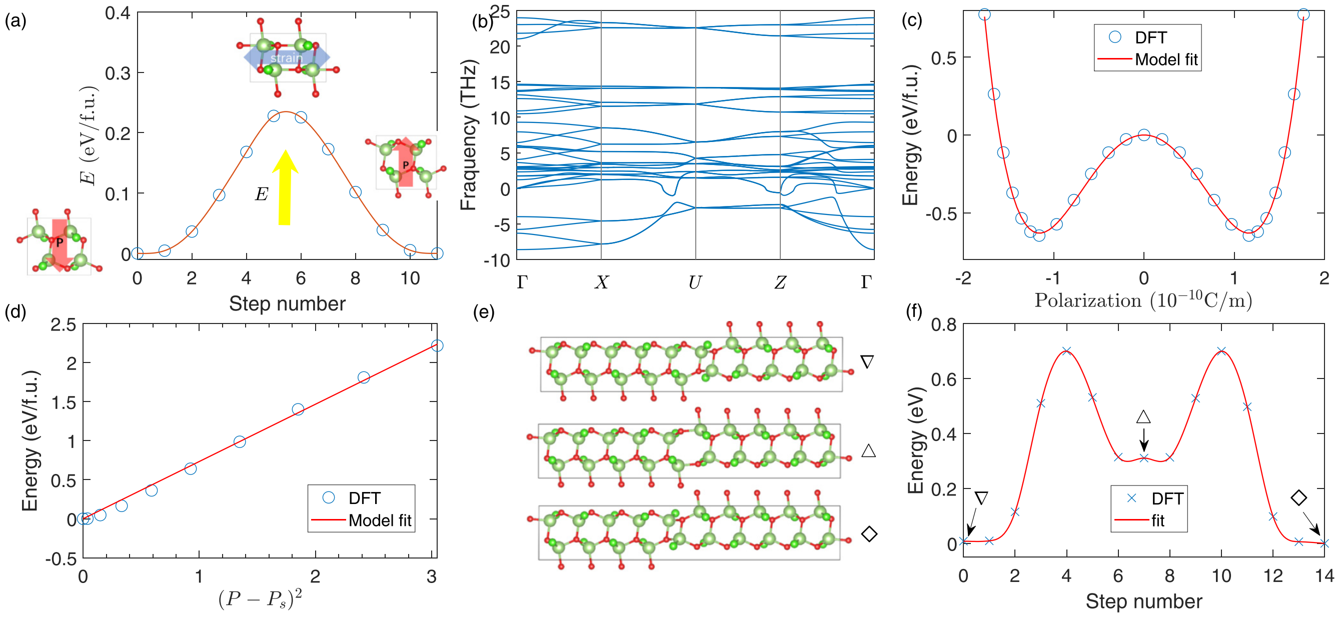

FIG. 3. (a) The polarization reversal kinetic pathway of GaOCl monolayer with corresponding structures in the insets, where the energy barrier is about 0.221 eV per f.u. (b) The calculated phonon dispersion spectrum of the intermediate state with fixed lattice. (c) The calculated and fitted double-well potential of GaOCl monolayer as a function of the polarization. (d) The calculated and fitted dipole-dipole interaction of GaOCl monolayer. (e) The snapshots of structures with corresponding ferroelectric domains during the kinetic pathway of domain wall motion of monolayer GaOCl in (f).

and ultrathin thickness. The electron density distributions at HOMO and LOMO are plotted in Fig. 2(f). We can see that, the HOMO is mainly contributed by $2p$ orbitals of O, and the LUMO is mainly contributed by the $3p$ orbitals of Cl. Therefore the ultrawide band gap for monolayer GaOCl is attributed to the high electronegativity of oxygen and chlorine.

C. Ferroelectricity of GaOCl monolayer

A macroscopic polarization emerges in GaOCl monolayer with $Pca2_1$ symmetry because of its broken centrosymmetry and semiconductor features. We thus study the polarization reversal kinetic pathway of GaOCl monolayer. The whole dynamic path of polarization reversion can be described as follows. Firstly, the low-symmetrical ferroelectric phase evolves towards high-symmetrical paraelectric structure under the external electric field. During this process, the lattice constant along a axis expands, the lattice constant along c axis contracts, and the Ga-O network transitions from the quasihexagonal structure in the left inset of Fig. 3(a) to the quasitetragonal structure in the up inset of Fig. 3(a) with chloride atoms straightened along b axis. Secondly, the high-symmetrical paraelectric structure evolves towards low-symmetrical ferroelectric phase spontaneously through an opposite symmetric process along the gradient of the potential energy surface. In the end, the macroscopic electric polarization is reversed in the right inset of Fig. 3(a). During the polarization reversal the energy barrier is about 0.221 eV per formula unit (f.u.). This moderate energy barrier indicates the macroscopic electric polarization reversion in GaOCl monolayer is feasible via an appropriate external electric field.

The unstable phonon frequencies associated with zone-center polar modes in the ideal high-symmetry prototype phase of ferroelectrics are often identified to illustrate displacive instabilities [36]. Spontaneous polarization emerges during the structural phase transition process from a high-symmetry nonpolar structure to a low-symmetry polar structural phase with the decreasing temperature. We calculate the phonon dispersion spectrum of the high symmetrical paraelectric structure and plot the result in Fig. 3(b). The existence of imaginary frequency phonon (soft optical mode) indicates that the polarization of ferroelectric GaOCl monolayer arises from the lattice network distortion of the high-symmetrical structure with a symmetry breaking.

Ferroelectric phase transition is a key problem in conventional proper ferroelectrics [128–130]. The Curie temperature for ferroelectric transitions in GaOCl monolayer can be predicted from the Landau free energy (F) model, where $F=\sum_i[(A/2)P_i^2+(B/4)P_i^4+(C/6)P_i^6]+(D/2)\sum_{\langle i,j\rangle}(P_i-P_j)^2$, with the polarization P_i of the unit cell at position i and the parameters A, B, C, and D determined from the first-principles calculations. The first three terms are contributed by the energy from the second, fourth, and sixth orders of the local modes, which describe the anharmonic double well free energy. The last term reflects the contribution of the nearest neighbor coupling of local modes. Firstly, we calculate the free energy as a function of the polarization and plot the energy curve in Fig. 3(c). The calculated polarization is ensured on the same branch without skipping polarization quantum, and the spontaneous polarization is about 1.16×10^{-10} C/m. We use the anharmonic double well free energy model to fit the calculated curve and obtain parameters $A=-7.08$, $B=4.31$, and $C=0.71$ with corresponding units such that the free energy is in units of eV per unit cell. Note that per unit cell of GaOCl monolayer has 4 dipole, and hence these parameters A, B, and C need to be

TABLE I. Ferroelectric polarization P in unit of 10^{-10} C/m of monolayer GaOCl at different temperatures simulated by MD or MC method.

$T\,(K)$	100	300	500	700	900	1100
P_{MD}	1.0196	1.2161	1.0399	1.2021	1.1558	1.0400
P_{MC}	1.1585	1.1574	1.1560	1.1549	1.1536	1.1525

divided by 4 so that the energy unit is eV per formula unit with one dipole. Secondly, we calculate the free energy only contributed by the local mode coupling and plot the result in Fig. 3(d). We use the linear relationship between F and $(P_i - \langle P_j \rangle)^2$ to fit the free energy, and obtain the coupling strength parameter $D = 1.46$ such that the free energy is in units of eV per unit cell as well.

To obtain the ferroelectric Curie temperature of GaOCl monolayer, we use the *ab initio* molecular dynamics to compute spontaneous polarizations at different temperatures, as listed in Table I. On the other hand, we also apply the Monte Carlo simulation based on the Landau free energy model to compute the spontaneous polarizations at different temperatures and also list the results in Table I for comparisons. The spontaneous polarization does not change significantly even though the temperature rises to the melting point. This result is also consistent with the high energy barrier of domain wall motions in Figs. 3(e) and 3(f). Therefore GaOCl monolayer has an excellent stability of high temperature ferroelectricity.

D. Superferroelasticity of GaOCl monolayer

Due to their membrane features, 2D materials can usually sustain relatively large strain, which can be induced by mechanical loadings or substrate engineering. Layered metal oxyhalides have four usual structural types with *Pmmn*, *Pca*2$_1$, *P*4/*nmm*, *P*6$_3$/*mcm* symmetries, and these structures can be transformed from each other by changing the ratio of the M^{3+} ionic radius to the O^{2-} ionic radius [123]. The largely tunable ionic radius ration in a continuous way allows various structural phase transitions. Strain can play a similar role in changing the ratio $r_{M^{3+}}/r_{O^{2-}}$ and transform the structural phases of GaOCl monolayer. Therefore GaOCl monolayer may exhibit various structural phase transitions which possibly enable a remarkable ferroelasticity phenomenon. We use the SSNEB method to investigate the possible ferroelastic phase transition in GaOCl monolayer. The obtained results are presented in Fig. 4 and these processes are described as follows.

Process 1. The structural symmetry changes from the initial *Pca*2$_1$ to *Pmmn* through an intermediate phase with an energy barrier of 0.5 eV/f.u. (or 0.17 eV/atom). The *a*-directional lattice constants of the intermediate and *Pmmn* phases are 6.23 and 6.51 Å, respectively.

Process 2. The structural symmetry changes from *Pmmn* to *P*4/*nmm* firstly, and then transition back to *Pmmn* but with the orientation of a 90° rotation, namely, *PmmnR*90°. During this process, the energy barrier is 0.13 eV/f.u. (or 0.04 eV/atom), and the *a*-directional lattice constants of *P*4/*nmm* and *PmmnR*90° phases are 7.35 and 7.64 Å, respectively.

Process 3. The structural symmetry transitions from *PmmnR*90° back to *Pca*2$_1$*R*90°, through a larger energy barrier of 0.58 eV/f.u. (or 0.19 eV/atom). The *a*-directional lattice constant of *Pca*2$_1$*R*90° is 10.30 Å.

The feasibility of such a stretching process is further examined by comparing the energy profile and stress-strain curve [131] for different phases of GaOCl monolayer.

In process 1 from *Pca*2$_1$ to *Pmmn*, the structure does not fracture before reaching the energy degeneracy point, at which the lattice constant is equals to 6.02 Å corresponding to a strain of 4.88% with respect to the lattice constant 5.74 Å of *Pca*2$_1$, and the stress is equals to 2 N/m respectively, as shown in Figs. 5(a) and 5(d).

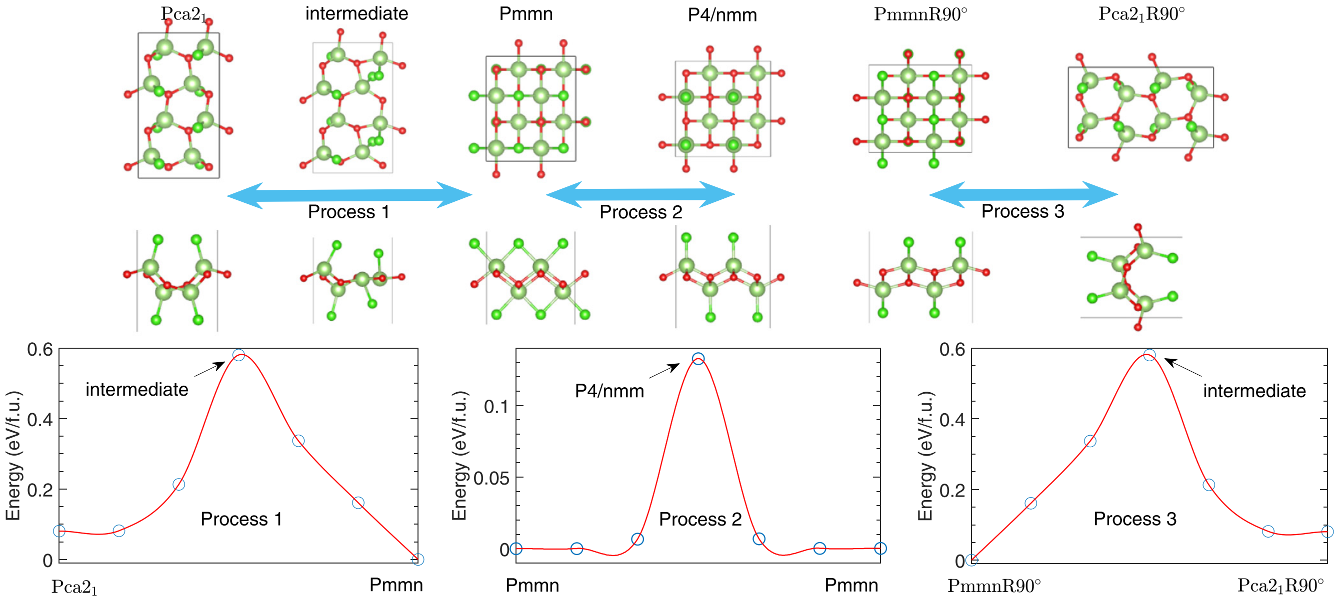

FIG. 4. Three ferroelastic phase transition processes driven by the uniaxial strain along double arrows in the top panel, with energy varying during processes 1–3 in the bottom panel, where circle points are calculated from DFT and red lines are from the modified Bezier fitting.

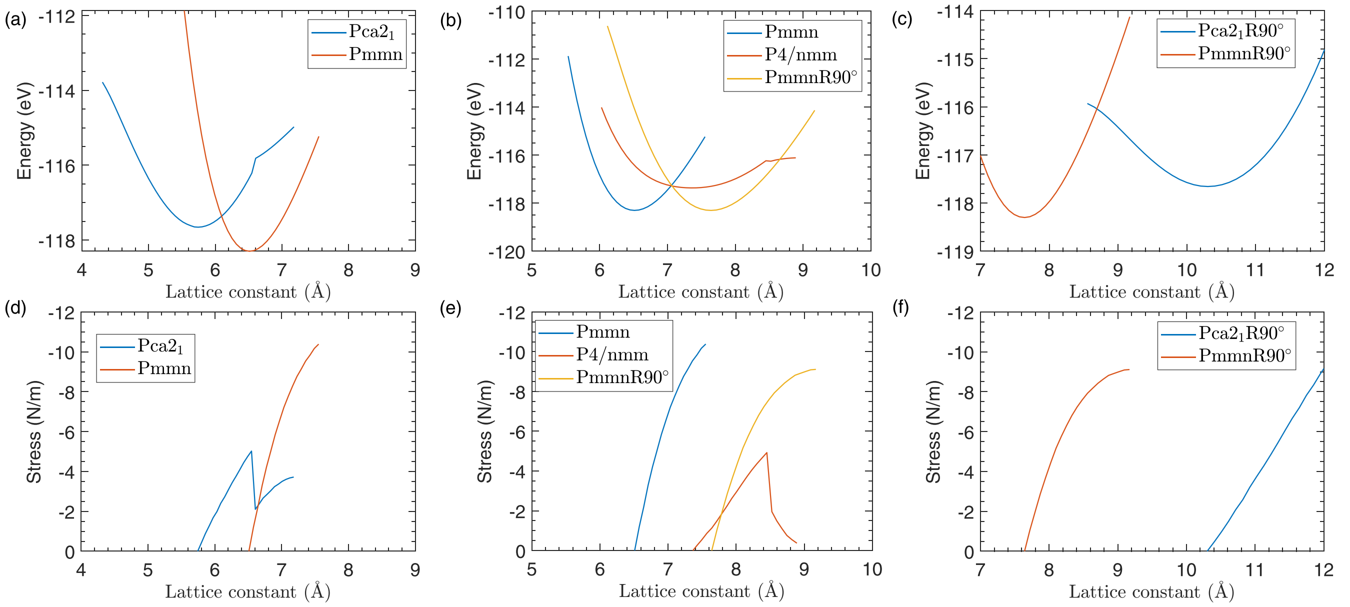

FIG. 5. Calculated energy (up panel) and stress (down panel) as a function of lattice constant in [(a) and (d)] for $Pca2_1$ and *Pmmn*, in [(b) and (e)] for *Pmmn*, *P*4/*nmm*, and *PmmnR*90°, and in [(c) and (f)] for $Pca2_1R90°$ and *PmmnR*90°.

In process 2 from *Pmmn* to P4/nmm, the structure does either not fracture before reaching the energy degeneracy point, where the lattice constant is equal to 7.03 Å corresponding to a strain 16.78 % compared with *Pmmn* or a strain 22.47% compared with $Pca2_1$, and the stress is equal to 7.2 N/m as shown in Figs. 5(b) and 5(e).

In process 3 from *Pmmn* R 90° to $Pca2_1R90°$, the structure has no fractures before arriving the energy degeneracy point, where the lattice constant is equal to 8.66Å corresponding to a strain 13.35% with respect to *Pmmn* R 90° or a strain 50.9% compared with $Pca2_1$, and the stress is equal to 8.2 N/m, as shown in Figs. 5(c) and 5(f).

For all the three processes, when the applied strain exceeds the energy degeneracy point, the later structural phase is more energy favorable, and thus the ferroelastic phase transition tends to proceed spontaneously. The very large strain and robust structural transitions without fractures indicates that monolayer GaOCl is superferroelastic. We also note that, the calculated phonon spectrum of the *Pmmn* phase with lower energy shows a very small imaginary frequency around Γ, and this means that the *Pmmn* phase is most likely to be dynamically stable, but there is relatively large energy barrier with about 0.5 eV/f.u. as shown in Fig. 4.

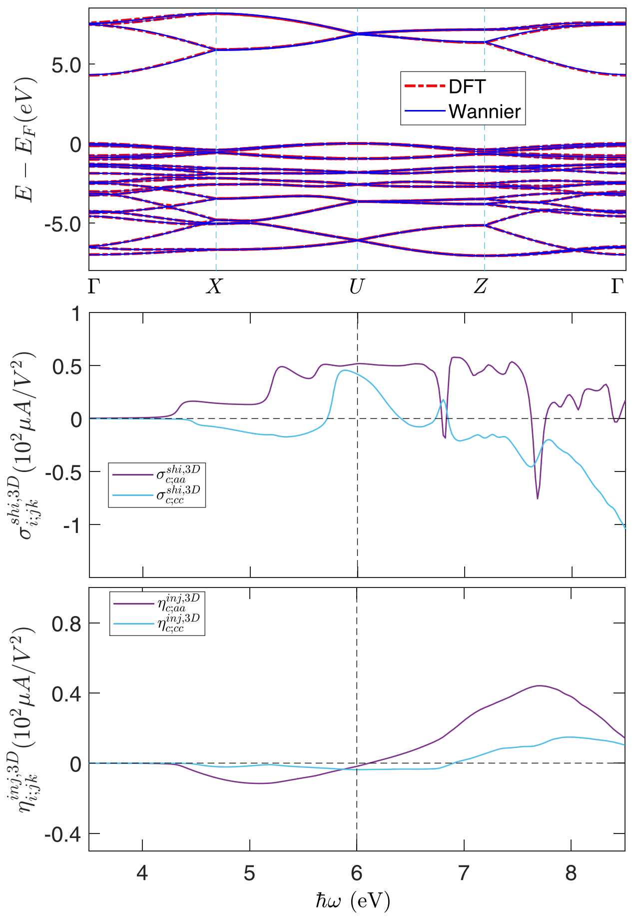

FIG. 6. Band structures from DFT calculation and Wannier interpolation for GaOCl monolayer (top). Nonlinear optical conductivities $\sigma^{shi,3D}_{i;jk}$ for shift current (middle) and $\eta^{inj,3D}_{i;jk}$ for injection current (bottom) in GaOCl monolayer as a function of photon energy $\hbar\omega$.

E. Nonlinear optical conductivity of GaOCl monolayer

As shown in Fig. 1, there is an obvious inversion symmetry breaking in the *bc* plane from the view of *a* axis. The broken inversion symmetry enables the ferroelectric polarization along the *c* axis. Owing to the symmetry requirements from the space group $Pca2_1$[132], we need to calculate these nonlinear optical conductivities with a fixed current direction along the polarization direction for 2D materials [70,118–120], i.e., $\sigma^{shi}_{c;aa}$, $\sigma^{shi}_{c;bb}$, $\sigma^{shi}_{c;cc}$, $\sigma^{inj}_{c;aa}$, $\sigma^{inj}_{c;bb}$, and $\sigma^{inj}_{c;cc}$. However, within the Wannier tight-binding model, the tensorial components with the index of *b* denoting the direction of the vacuum

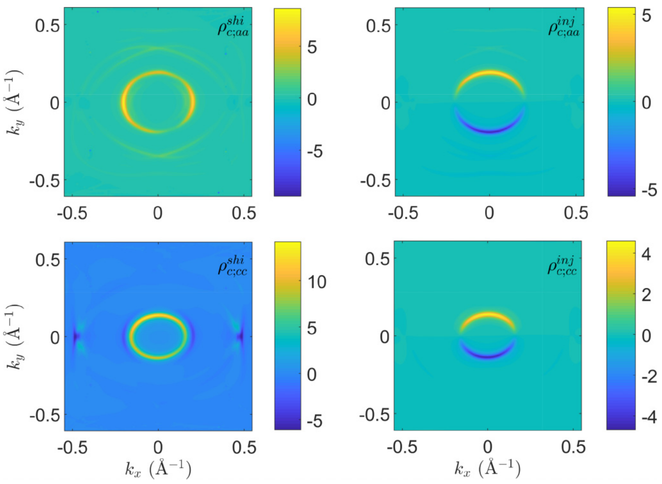

FIG. 7. Susceptibility densities $\rho^{shi}_{i;jk}(\mathbf{k})$ for shift current and $\rho^{inj}_{i;jk}(\mathbf{k})$ for injection current in GaOCl monolayer in unit of $\pi e/\hbar$ at $\hbar\omega = 6$ eV as denoted by the vertical dashed lines in Fig. 6. All individual subfigures have the same labels of k_x and k_y axes in unit of Å^{-1}.

layer are not calculated due to the lack of the wave vector component k_b, i.e., without the periodicity along b direction.

Figure 6 shows the band structures from the Wannier interpolation and the nonlinear optical conductivities as a function of photon energy $\hbar\omega$ with $\hbar\tau^{-1} = 0.02$ eV for GaOCl monolayer, where the photon energy range is set from 3.5 to 8.5 eV according to the band gap and the effective energy window from the Wannier interpolation. We rescale these nonlinear optical conductivities to $\sigma^{shi,3D}_{i;jk}$ and $\eta^{inj,3D}_{i;jk}$ by the factor t_u/t_m [119,120], where $t_u = 30$ Å is the slab thickness of unit cell along b direction, and $t_m = 5.79$ Å is the single-layer thickness of GaOCl. The shift and injection conductivities have a large nonlinear response magnitude with the order of 10^2 μA/V^2, which is comparable to that of other 2D semiconductors and [70–73,119,120] and bulk GaAs with the maximum magnitude around 30 μA/V^2 [133]. Especially, those large nonlinear optical current responses are inside deep-ultraviolet frequency range higher than 4.28 eV, enabling applications in integrated ultraviolet optoelectronic devices.

Although the sapce group $Pca2_1$ makes $\sigma^{shi}_{c;aa}$, $\sigma^{shi}_{c;cc}$, $\sigma^{inj}_{c;aa}$, and $\sigma^{inj}_{c;cc}$ as independent components, they can also be zero or small value for some special photon energy range, as shown in Fig. 6. To illustrate how the these large or small nonlinear optical susceptibilities emerge, we further calculate the susceptibility densities $\rho^{shi}_{i;jk}(\mathbf{k})$ for shift current and $\rho^{inj}_{i;jk}(\mathbf{k})$ for injection current in Fig. 7, where the nonlinear optical susceptibilities are determined by $\sigma^{shi}_{i;jk} = \int_{\mathbf{k}} \rho^{shi}_{i;jk}(\mathbf{k})$ and $\eta^{inj}_{i;jk} = \int_{\mathbf{k}} \rho^{inj}_{i;jk}(\mathbf{k})$ in Eq. (1) and the photon energy is given at $\hbar\omega = 6$ eV as an example. As we see, the two susceptibility densities $\rho^{shi}_{c;aa}(\mathbf{k})$ and $\rho^{shi}_{c;cc}(\mathbf{k})$ show even distributions for $\mathbf{k}$ and hence their integrals on $\mathbf{k}$ enable the remarkable shift current. For injection current at $\hbar\omega = 6$ eV, $\rho^{inj}_{c;aa}(\mathbf{k})$ and $\rho^{inj}_{c;cc}(\mathbf{k})$ have the odd distributions about $\mathbf{k}$, supporting small injection currents, as shown in down panel of Fig. 6. At last, we figure that the projection procedure within the Wannier function interpolation might violate the original symmetry and lead to relatively small nonzero values for these components which should be zero from symmetry requirements. In future, calculations on nonlinear optical conductivities including symmetrized wannierization need to be further performed with the same crystal symmetries [134–136].

IV. CONCLUSION

We use cleavage simulation, molecular dynamics simulation and phonon spectrum computations within the first-principles calculations to find that GaOCl monolayer is a new 2D metal chalcogens halide, which is thermodynamically stable from room temperature to 1000 K. The broken inversion symmetry and wide direct band gap of 4.28 eV for GaOCl monolayer enable ferroelectric spontaneous polarization. We further apply polarization reversal kinetic simulation, Landau free energy model calculations with dipole-dipole interaction and ab initio molecular dynamics together with Monte Carlo simulation to verify that GaOCl monolayer is a displacive ferroelectricity with high phase transition Curie temperature more than its melting point. The calculated energy-strain relation and stress-strain relation within the SSNEB method show that GaOCl monolayer can sustain various structural phase transition processes without fractures and hence exhibits a superferroelasticity property. The time-dependent perturbation theoretical calculation shows that GaOCl monolayer possesses large deep-ultraviolet shift and injection current responses as a consequence of nonzero susceptibility densities with even distributions of $\mathbf{k}$. Our theoretical results suggest that GaOCl monolayer is a good candidate for applications on novel integrated ultrathin ferroelectric electronics, superferroelastic devices, and deep-ultraviolet nonlinear optoelectronics.

ACKNOWLEDGMENTS

This work is supported by the National Natural Science Foundation of China (Nos. 12174291 and 12247101), the 111 Project (Grant No. B20063), and the National Key Research and Development Program of China (Grant No. 2022YFA1402704).

---

[1] L. W. Martin and A. M. Rappe, Nat. Rev. Mater. **2**, 16087 (2016).
[2] M. Wu and P. Jena, WIREs Comput. Mol. Sci. **8**, e1365 (2018).
[3] C. Cui, F. Xue, W.-J. Hu, and L.-J. Li, npj 2D Materials and Applications **2**, 18 (2018).
[4] M. Osada and T. Sasaki, APL Mater. **7**, 120902 (2019).
[5] X. Tang and L. Kou, J. Phys. Chem. Lett. **10**, 6634 (2019).
[6] T. Hu and E. Kan, WIREs Comput. Mol. Sci. **9**, e1409 (2019).
[7] Z. Guan, H. Hu, X. Shen, P. Xiang, N. Zhong, J. Chu, and C. Duan, Adv. Electron. Mater. **6**, 1900818 (2020).

[8] M. Wu, ACS Nano **15**, 9229 (2021).
[9] J. Shang, X. Tang, and L. Kou, WIREs Comput. Mol. Sci. **11**, e1496 (2021).
[10] L. Qi, S. Ruan, and Y.-J. Zeng, Adv. Mater. **33**, 2005098 (2021).
[11] J. Chu, Y. Wang, X. Wang, K. Hu, G. Rao, C. Gong, C. Wu, H. Hong, X. Wang, K. Liu *et al.*, Adv. Mater. **33**, 2004469 (2021).
[12] S. Barraza-Lopez, B. M. Fregoso, J. W. Villanova, S. S. Parkin, and K. Chang, Rev. Mod. Phys. **93**, 011001 (2021).
[13] Z. Liu, L. Deng, and B. Peng, Nano Res. **14**, 1802 (2021).
[14] H. Qiao, C. Wang, W. S. Choi, M. H. Park, and Y. Kim, Mater. Sci. Eng. R **145**, 100622 (2021).
[15] T. Jin, J. Mao, J. Gao, C. Han, K. P. Loh, A. T. Wee, and W. Chen, ACS Nano **16**, 13595 (2022).
[16] X. Jin, Y.-Y. Zhang, and S. Du, Fundamental Research **3**, 322 (2023).
[17] C. Wang, L. You, D. Cobden, and J. Wang, Nat. Mater. **22**, 542 (2023).
[18] D. Zhang, P. Schoenherr, P. Sharma, and J. Seidel, Nat. Rev. Mater. **8**, 25 (2023).
[19] S. Li, F. Wang, Y. Wang, J. Yang, X. Wang, X. Zhan, J. He, and Z. Wang, Adv. Mater. **35**, 2301472 (2023).
[20] S. Lin, G. Zhang, Q. Lai, J. Fu, W. Zhu, and H. Zeng, Adv. Funct. Mater., **33** 2304139 (2023).
[21] K. Chang, J. Liu, H. Lin, N. Wang, K. Zhao, A. Zhang, F. Jin, Y. Zhong, X. Hu, W. Duan *et al.*, Science **353**, 274 (2016).
[22] F. Liu, L. You, K. L. Seyler, X. Li, P. Yu, J. Lin, X. Wang, J. Zhou, H. Wang, H. He *et al.*, Nat. Commun. **7**, 1 (2016).
[23] Y. Zhou, D. Wu, Y. Zhu, Y. Cho, Q. He, X. Yang, K. Herrera, Z. Chu, Y. Han, M. C. Downer *et al.*, Nano Lett. **17**, 5508 (2017).
[24] J. Xiao, H. Zhu, Y. Wang, W. Feng, Y. Hu, A. Dasgupta, Y. Han, Y. Wang, D. A. Muller, L. W. Martin *et al.*, Phys. Rev. Lett. **120**, 227601 (2018).
[25] S. Yuan, X. Luo, H. L. Chan, C. Xiao, Y. Dai, M. Xie, and J. Hao, Nat. Commun. **10**, 1775 (2019).
[26] L. You, F. Liu, H. Li, Y. Hu, S. Zhou, L. Chang, Y. Zhou, Q. Fu, G. Yuan, S. Dong *et al.*, Adv. Mater. **30**, 1803249 (2018).
[27] Z. Fei, W. Zhao, T. A. Palomaki, B. Sun, M. K. Miller, Z. Zhao, J. Yan, X. Xu, and D. H. Cobden, Nature (London) **560**, 336 (2018).
[28] Z. Zheng, Q. Ma, Z. Bi, S. de La Barrera, M.-H. Liu, N. Mao, Y. Zhang, N. Kiper, K. Watanabe, T. Taniguchi *et al.*, Nature (London) **588**, 71 (2020).
[29] K. Yasuda, X. Wang, K. Watanabe, T. Taniguchi, and P. Jarillo-Herrero, Science **372**, 1458 (2021).
[30] M. Vizner Stern, Y. Waschitz, W. Cao, I. Nevo, K. Watanabe, T. Taniguchi, E. Sela, M. Urbakh, O. Hod, and M. Ben Shalom, Science **372**, 1462 (2021).
[31] X. Wang, K. Yasuda, Y. Zhang, S. Liu, K. Watanabe, T. Taniguchi, J. Hone, L. Fu, and P. Jarillo-Herrero, Nat. Nanotechnol. **17**, 367 (2022).
[32] C. B. Park, A. Shahee, K.-T. Kim, D. R. Patil, S. A. Guda, N. Ter-Oganessian, and K. H. Kim, Adv. Electron. Mater. **8**, 2101072 (2022).
[33] W. Li, X. Zhang, J. Yang, S. Zhou, C. Song, P. Cheng, Y.-Q. Zhang, B. Feng, Z. Wang, Y. Lu *et al.*, Nat. Commun. **14**, 2757 (2023).
[34] J. Gou, H. Bai, X. Zhang, Y. L. Huang, S. Duan, A. Ariando, S. A. Yang, L. Chen, Y. Lu, and A. T. S. Wee, Nature (London) **617**, 67 (2023).
[35] S. N. Shirodkar and U. V. Waghmare, Phys. Rev. Lett. **112**, 157601 (2014).
[36] R. Fei, W. Kang, and L. Yang, Phys. Rev. Lett. **117**, 097601 (2016).
[37] L.-F. Lin, Y. Zhang, A. Moreo, E. Dagotto, and S. Dong, Phys. Rev. Lett. **123**, 067601 (2019).
[38] K. Liu, J. Lu, S. Picozzi, L. Bellaiche, and H. Xiang, Phys. Rev. Lett. **121**, 027601 (2018).
[39] Q.-J. Ye, Z.-Y. Liu, Y. Feng, P. Gao, and X.-Z. Li, Phys. Rev. Lett. **121**, 135702 (2018).
[40] M. Wu and J. Li, Proc. Natl. Acad. Sci. USA **118**, e2115703118 (2021).
[41] J. Ji, G. Yu, C. Xu, and H. Xiang, Phys. Rev. Lett. **130**, 146801 (2023).
[42] L. Yang, S. Ding, J. Gao, and M. Wu, Phys. Rev. Lett. **131**, 096801 (2023).
[43] P. Tang and G. E. W. Bauer, Phys. Rev. Lett. **130**, 176801 (2023).
[44] L.-P. Miao, N. Ding, N. Wang, C. Shi, H.-Y. Ye, L. Li, Y.-F. Yao, S. Dong, and Y. Zhang, Nat. Mater. **21**, 1158 (2022).
[45] F. Sui, M. Jin, Y. Zhang, R. Qi, Y.-N. Wu, R. Huang, F. Yue, and J. Chu, Nat. Commun. **14**, 36 (2023).
[46] P. Meng, Y. Wu, R. Bian, E. Pan, B. Dong, X. Zhao, J. Chen, L. Wu, Y. Sun, Q. Fu *et al.*, Nat. Commun. **13**, 7696 (2022).
[47] L. Li and M. Wu, ACS Nano **11**, 6382 (2017).
[48] C. Huang, Y. Du, H. Wu, H. Xiang, K. Deng, and E. Kan, Phys. Rev. Lett. **120**, 147601 (2018).
[49] J.-J. Zhang, L. Lin, Y. Zhang, M. Wu, B. I. Yakobson, and S. Dong, J. Am. Chem. Soc. **140**, 9768 (2018).
[50] Y. Lai, Z. Song, Y. Wan, M. Xue, C. Wang, Y. Ye, L. Dai, Z. Zhang, W. Yang, H. Du *et al.*, Nanoscale **11**, 5163 (2019).
[51] T. Zhong, X. Li, M. Wu, and J.-M. Liu, Natl. Sci. Rev. **7**, 373 (2020).
[52] C. Xu, P. Chen, H. Tan, Y. Yang, H. Xiang, and L. Bellaiche, Phys. Rev. Lett. **125**, 037203 (2020).
[53] X. Liu, A. P. Pyatakov, and W. Ren, Phys. Rev. Lett. **125**, 247601 (2020).
[54] J. Zhang, Y. Zhou, F. Wang, X. Shen, J. Wang, and X. Lu, Phys. Rev. Lett. **129**, 117603 (2022).
[55] M. Wu and X. C. Zeng, Nano Lett. **16**, 3236 (2016).
[56] L. Kou, Y. Ma, C. Tang, Z. Sun, A. Du, and C. Chen, Nano Lett. **16**, 7910 (2016).
[57] W. Li and J. Li, Nat. Commun. **7**, 10843 (2016).
[58] H. Wang and X. Qian, 2D Mater. **4**, 015042 (2017).
[59] B. Xu, H. Xiang, J. Yin, Y. Xia, and Z. Liu, Nanoscale **10**, 215 (2018).
[60] T. Zhang, Y. Liang, X. Xu, B. Huang, Y. Dai, and Y. Ma, Phys. Rev. B **103**, 165420 (2021).
[61] C. Xu, J. Mao, X. Guo, S. Yan, Y. Chen, T. W. Lo, C. Chen, D. Lei, X. Luo, J. Hao *et al.*, Nat. Commun. **12**, 3665 (2021).
[62] X. Xuan, W. Guo, and Z. Zhang, Phys. Rev. Lett. **129**, 047602 (2022).
[63] X. Xu, Y. Ma, B. Huang, and Y. Dai, Phys. Chem. Chem. Phys. **21**, 7440 (2019).
[64] X. Lu, Z. Chen, Y. Cao, Y. Tang, R. Xu, S. Saremi, Z. Zhang, L. You, Y. Dong, S. Das *et al.*, Nat. Commun. **10**, 3951 (2019).

[65] Z. Tu and M. Wu, Sci. Bull. **65**, 147 (2020).

[66] S. Guan, C. Liu, Y. Lu, Y. Yao, and S. A. Yang, Phys. Rev. B **97**, 144104 (2018).

[67] H. Shen, J. Liu, K. Chang, and L. Fu, Phys. Rev. Appl. **11**, 024048 (2019).

[68] S. M. Young and A. M. Rappe, Phys. Rev. Lett. **109**, 116601 (2012).

[69] N. Nagaosa and T. Morimoto, Adv. Mater. **29**, 1603345 (2017).

[70] T. Rangel, B. M. Fregoso, B. S. Mendoza, T. Morimoto, J. E. Moore, and J. B. Neaton, Phys. Rev. Lett. **119**, 067402 (2017).

[71] N. Ogawa, M. Sotome, Y. Kaneko, M. Ogino, and Y. Tokura, Phys. Rev. B **96**, 241203(R) (2017).

[72] S. R. Panday, S. Barraza-Lopez, T. Rangel, and B. M. Fregoso, Phys. Rev. B **100**, 195305 (2019).

[73] H. Wang and X. Qian, Sci. Adv. **5**, eaav9743 (2019).

[74] J. Orenstein, J. Moore, T. Morimoto, D. Torchinsky, J. Harter, and D. Hsieh, Annu. Rev. Condens. Matter Phys. **12**, 247 (2021).

[75] Q. Ma, A. G. Grushin, and K. S. Burch, Nat. Mater. **20**, 1601 (2021).

[76] C. Bao, P. Tang, D. Sun, and S. Zhou, Nat. Rev. Phys. **4**, 33 (2022).

[77] A. Autere, H. Jussila, Y. Dai, Y. Wang, H. Lipsanen, and Z. Sun, Adv. Mater. **30**, 1705963 (2018).

[78] X. Wen, Z. Gong, and D. Li, InfoMat **1**, 317 (2019).

[79] H. An, Y. Du, T. Wang, C. Wang, W. Hao, and J. Zhang, Rare Metals **27**, 243 (2008).

[80] L. Zhao, X. Zhang, C. Fan, Z. Liang, and P. Han, Physica B: Condens. Matter **407**, 3364 (2012).

[81] L. Ye, J. Liu, C. Gong, L. Tian, T. Peng, and L. Zan, ACS Catal. **2**, 1677 (2012).

[82] H. Cheng, B. Huang, and Y. Dai, Nanoscale **6**, 2009 (2014).

[83] L. Ye, Y. Su, X. Jin, H. Xie, and C. Zhang, Environ. Sci. Nano **1**, 90 (2014).

[84] J. Li, Y. Yu, and L. Zhang, Nanoscale **6**, 8473 (2014).

[85] Y. Yang, C. Zhang, C. Lai, G. Zeng, D. Huang, M. Cheng, J. Wang, F. Chen, C. Zhou, and W. Xiong, Adv. Colloid Interface Sci. **254**, 76 (2018).

[86] K. Xu, L. Wang, X. Xu, S. X. Dou, W. Hao, and Y. Du, Energy Storage Materials **19**, 446 (2019).

[87] M. Arumugam, T. S. Natarajan, T. Saelee, S. Praserthdam, M. Ashokkumar, and P. Praserthdam, Chemosphere **282**, 131054 (2021).

[88] S. Vinoth, W.-J. Ong, and A. Pandikumar, Coord. Chem. Rev. **464**, 214541 (2022).

[89] X. Wu, H. L. Tan, C. Zhang, Z. Teng, Z. Liu, Y. H. Ng, Q. Zhang, and C. Su, Prog. Mater. Sci. **133**, 101047 (2022).

[90] Z. Ali, J. Ma, M. Hong, and R. Sun, J. Mater. Chem. A **11**, 3297 (2023).

[91] N. Miao, B. Xu, L. Zhu, J. Zhou, and Z. Sun, J. Am. Chem. Soc. **140**, 2417 (2018).

[92] X. Qing, H. Li, C. Zhong, P. Zhou, Z. Dong, and J. Liu, Phys. Chem. Chem. Phys. **22**, 17255 (2020).

[93] Q.-Y. Rong, A.-M. Hu, X.-H. Zhang, L.-L. Wang, and W.-Z. Xiao, J. Magn. Magn. Mater. **515**, 167310 (2020).

[94] X. Cai, Z. Xu, H. Zhou, J. Ren, N. Li, S. Meng, S.-H. Ji, and X. Chen, Phys. Rev. Mater. **4**, 064003 (2020).

[95] L. Craco, M. Laad, and E. Müller-Hartmann, J. Phys.: Condens. Matter **18**, 10943 (2006).

[96] Y. Feng, R. Peng, Y. Dai, B. Huang, L. Duan, and Y. Ma, Appl. Phys. Lett. **119**, 173103 (2021).

[97] H.-P. You, N. Ding, J. Chen, and S. Dong, Phys. Chem. Chem. Phys. **22**, 24109 (2020).

[98] S. Xu, F. Jia, G. Zhao, W. Wu, and W. Ren, J. Mater. Chem. C **9**, 9130 (2021).

[99] L. Zhao, M. T. Fernández-Díaz, L. H. Tjeng, and A. C. Komarek, Sci. Adv. **2**, e1600353 (2016).

[100] G. Villalpando, A. M. Ferrenti, R. Singha, X. Song, G. Cheng, N. Yao, and L. M. Schoop, ACS Nano **16**, 13814 (2022).

[101] S. Wang, J. Wang, and M. Khazaei, Phys. Chem. Chem. Phys. **22**, 11731 (2020).

[102] Y. Zeng, P. Gu, Z. Zhao, B. Zhang, Z. Lin, Y. Peng, W. Li, W. Zhao, Y. Leng, P. Tan *et al.*, Adv. Mater. **34**, 2108847 (2022).

[103] W. Li, N. Miao, J. Zhou, and Z. Sun, J. Mater. Chem. C **9**, 547 (2021).

[104] T. Das and S. Datta, Nanoscale Adv. **2**, 1090 (2020).

[105] J. He, P. Lyu, and P. Nachtigall, Catal. Today **340**, 178 (2020).

[106] A. Devi, P. Ahluwalia, A. Kumar, P. Contreras *et al.*, Mater. Today: Proc. (2023).

[107] M. Noor-A-Alam and M. Nolan, Nanoscale **14**, 11676 (2022).

[108] S. Jiang, H. Yin, and G.-P. Zheng, Nanoscale **14**, 11369 (2022).

[109] P. E. Blochl, Phys. Rev. B **50**, 17953 (1994).

[110] G. Kresse and J. Furthmüller, Phys. Rev. B **54**, 11169 (1996).

[111] G. Kresse and D. Joubert, Phys. Rev. B **59**, 1758 (1999).

[112] J. P. Perdew, K. Burke, and M. Ernzerhof, Phys. Rev. Lett. **77**, 3865 (1996).

[113] M. Methfessel and A. T. Paxton, Phys. Rev. B **40**, 3616 (1989).

[114] D. Sheppard, P. Xiao, W. Chemelewski, D. D. Johnson, and G. Henkelman, J. Chem. Phys. **136**, 074103 (2012).

[115] R. D. King-Smith and D. Vanderbilt, Phys. Rev. B **47**, 1651 (1993).

[116] J. Heyd and G. E. Scuseria, J. Chem. Phys. **120**, 7274 (2004).

[117] G. J. Martyna, M. L. Klein, and M. Tuckerman, J. Chem. Phys. **97**, 2635 (1992).

[118] A. M. Cook, B. M. Fregoso, F. De Juan, S. Coh, and J. E. Moore, Nat. Commun. **8**, 14176 (2017).

[119] C. Wang, X. Liu, L. Kang, B.-L. Gu, Y. Xu, and W. Duan, Phys. Rev. B **96**, 115147 (2017).

[120] J. Ibañez-Azpiroz, S. S. Tsirkin, and I. Souza, Phys. Rev. B **97**, 245143 (2018).

[121] J. Ahn, G.-Y. Guo, and N. Nagaosa, Phys. Rev. X **10**, 041041 (2020).

[122] A. A. Mostofi, J. R. Yates, G. Pizzi, Y.-S. Lee, I. Souza, D. Vanderbilt, and N. Marzari, Comput. Phys. Commun. **185**, 2309 (2014).

[123] T. R. Halbert, *Intercalation Chemistry of Metal Chalcogenohalides* (Academic Press, New York, 1982), p. 375.

[124] J. N. Coleman, M. Lotya, A. O'Neill, S. D. Bergin, P. J. King, U. Khan, K. Young, A. Gaucher, S. De, R. J. Smith *et al.*, Science **331**, 568 (2011).

[125] N. Medvedeva, O. Mryasov, Y. N. Gornostyrev, D. Novikov, and A. Freeman, Phys. Rev. B **54**, 13506 (1996).

[126] W. Wang, S. Dai, X. Li, J. Yang, D. J. Srolovitz, and Q. Zheng, Nat. Commun. **6**, 7853 (2015).

[127] H. Zhou, S. Alghmadi, M. Si, G. Qiu, and D. Y. Peide, IEEE Electron Device Lett. **37**, 1411 (2016).

[128] W. Zhong, D. Vanderbilt, and K. M. Rabe, Phys. Rev. Lett. **73**, 1861 (1994).

[129] I. C. Infante, J. Juraszek, S. Fusil, B. Dupé, P. Gemeiner, O. Diéguez, F. Pailloux, S. Jouen, E. Jacquet, G. Geneste *et al.*, Phys. Rev. Lett. **107**, 237601 (2011).

[130] Y. Yang, H. Mao, J. Wang, Q. Zhang, L. Jin, C. Wang, Y. Zhang, N. Su, F. Meng, Y. Yang *et al.*, Adv. Mater. **32**, 2003033 (2020).

[131] J. Tan, Y. Wang, Z. Wang, X. He, Y. Liu, B. Wang, M. I. Katsnelson, and S. Yuan, Nano Energy **65**, 104058 (2019).

[132] S. V. Gallego, J. Etxebarria, L. Elcoro, E. S. Tasci, and J. M. Perez-Mato, Acta Cryst. A **75**, 438 (2019).

[133] F. Nastos and J. E. Sipe, Phys. Rev. B **74**, 035201 (2006).

[134] R. Sakuma, Phys. Rev. B **87**, 235109 (2013).

[135] Q. Wu, S. Zhang, H.-F. Song, M. Troyer, and A. A. Soluyanov, Comput. Phys. Commun. **224**, 405 (2018).

[136] G.-X. Zhi, C. Xu, S.-Q. Wu, F. Ning, and C. Cao, Comput. Phys. Commun. **271**, 108196 (2022).

Correction: The name of the first author was misspelled and has been fixed.